RSC Advances

PAPER

View Article Online
View Journal | View Issue

Cite this: *RSC Adv.*, 2025, **15**, 29800

Electro/photo multi-energy triggered expanded graphite/polyethylene glycol composite phase change materials for wearable thermotherapy

Bui Van Phuoc,† Ho Phuong,† Le Thi Duy Hanh, Huynh Nguyen Anh Tuan, Minh Tam Le, Nguyen Ngoc Que Anh, Luong Thi Thao and Giang Tien Nguyen *

In this work, we combined expanded graphite (ExG) and polyethylene glycol (PEG) to fabricate composite phase change materials (CPCMs) with effective photo/electrothermal conversion and storage, potentially applied to thermotherapy. The CPCMs were studied with varying contents of PEG (60, 70, 80, and 90%), showing good leakage-proof ability at a PEG content of up to 90% and high crystallization fractions of 94.4–98.7%. These two factors promoted a high thermal energy storage capacity of 151.1 J g^{-1} for the fabricated CPCM90 (the CPCM with 90% PEG). The CPCMs also exhibited good cycling durability, high thermal stability, and elevated thermal conductivities of 3.201–7.683 W (m^{-1} K^{-1}), which were 11.6–27.9 times above that of pure PEG. The high electrical conductivity and light absorption of ExG allowed effective electro/photothermal conversion and storage for the CPCMs. For example, the CPCM90 could be heated from the ambient to 70 °C in 390 s, as applied with a low electrical energy of 1.5 V. It also exhibited a high photothermal conversion efficiency of 84.0% at a simulated solar radiation of 1000 W m^{-2}. The CPCM90 was further evaluated for practical thermotherapy application as a heat eye-patch, which could maintain temperatures within 40.0–42.5 °C for 37 min. This temperature range and duration were highly desired for eye relaxation and therapy of some eye issues.

Received 9th June 2025
Accepted 18th August 2025

DOI: 10.1039/d5ra04061b

rsc.li/rsc-advances

1. Introduction

Phase change materials (PCMs) offer a promising approach in thermotherapy due to their ability to absorb and release thermal energy at nearly constant temperatures, providing stable and controlled heat delivery over extended periods.[1,2] This makes them ideal for applications such as pain relief, post-surgical recovery, muscle and eye relaxation, menstrual pain management, physical therapy, and even veterinary and oncology care.[3–5] Their portability, energy independence, and customizable melting points make them convenient for both clinical and home use, while their reusability contributes to environmental sustainability. However, PCMs also exhibit limitations, including low thermal conductivity, liquid phase leakage, poor electrical conductivity, and poor solar absorption, restricting them in multimodal energy harvesting and practical thermotherapy applications.[6,7]

Integrating PCMs with functional porous supports (thermally conductive porous supports, electrically conductive porous supports, photothermal porous supports, *etc*) offers several key advantages that enhance the performance and applicability of thermal energy storage systems.[8–10] The porous structure provides a stable scaffold that helps contain the PCMs, reducing the risk of leakage during phase transitions.[11,12] The high thermal conductivity of porous supports improves thermal conductivity within the composites, enabling faster heat transfer and more efficient charging and discharging of thermal energy.[13,14] Additionally, the high electrical conductivity and/or high solar absorption of porous supports enable the energy conversion and storage for the composites.[3,15] However, these combinations also come with drawbacks. Several porous supports have pore sizes that are too large, so they can not provide sufficient capillary and surface tension forces to stabilize PCMs inside them, producing a poor loading capacity of PCMs.[16,17] The infiltration of PCM into the porous structure may reduce the overall latent heat storage capacity due to the reduced PCM volume. In addition, several porous supports with complicated production and expensive raw materials, such as Mxene,[18,19] graphene,[20,21] Ag nanoparticles,[22,23] and carbon nanotubes,[24,25] may also limit their scalability and practical applications. Consequently, it is essential to discover functional porous supports possessing suitable porous networks, multimodal energy conversion, high stability, and simple and low-cost production to enhance the thermal performance of PCMs.

Expanded graphite (ExG) is an ideal porous support for PCMs because it possesses a highly porous and interconnected structure with a large surface area, enhancing the impregnation

Faculty of Chemical and Food Technology, Ho Chi Minh City University of Technology and Education (HCMUTE), 1 Vo Van Ngan, Thu Duc, Ho Chi Minh City 700000, Vietnam. E-mail: ntgiang@hcmute.edu.vn

† These authors equally contributed to this work.

and retention of PCMs.[13,26] It also exhibits exceptional thermal conductivity, greatly improving heat transfer during charging and discharging cycles. Moreover, ExG exhibits excellent photothermal conversion capabilities, efficiently absorbing and converting solar radiation into thermal energy, which can then be stored in the PCM for later use.[27–29] In addition, its superior electrical conductivity potentially enables effective electrothermal conversion and storage for the composite PCMs, generating powerful and multifunctional support material for next-generation energy storage systems. In previously reported CPCMs, ExG has been used as thermal conductivity/photothermal additives in combination with other porous materials.[5,30–33] ExG has also been used as a sole thermal conductivity/photothermal porous support to integrate with various PCMs.[28,29,34–36] However, while the photothermal conversion of these ExG-based CPCMs has been well demonstrated, the electrothermal conversion and storage have remained largely unexplored. Additionally, to our knowledge, the practical performance of a CPCM based on ExG as a sole porous support in thermotherapy has not been discovered. These result in a knowledge gap on the multimodal energy conversion and the thermotherapy applicability of this thermal storage material type.

To be applicable in thermotherapy, a PCM should first have a phase change temperature appropriate to thermotherapy temperatures, which are categorized into high level (50–55 °C), mid level (40–50 °C), and low level (35–40 °C).[3,37] In this work, we used polyethylene glycol (PEG, MW = 6000 g mol^{-1}) as a PCM for its desired phase crystallization temperature (~44 °C), relatively high energy storage capacity (~190 J g^{-1}), biodegradability, high thermal stability, low cost, and high availability. PEG was impregnated into ExG at varying PEG contents of 60–90% to form multimodal thermal energy conversion and storage CPCMs, and their thermophysical properties were studied with the varying PEG contents. The microstructure, morphology, chemical compatibility, and crystallization behaviours were first characterized for the fabricated CPCMs. Then, the thermal properties, including phase change behaviours, thermal stability, thermal conductivity, and leakage-proof ability, were carefully studied. Finally, the multimodal energy conversion, including photothermal and electrothermal conversion, and practical thermotherapy application were investigated and discussed.

2. Materials and methods

2.1 Materials

Expandable graphite was bought from Sigma Aldrich (US). Polyethylene glycol (MW = 6000 g mol^{-1}) and absolute ethanol were purchased from Shanghai Zhanyun Chemical (China).

2.2 Fabrication of composite phase change materials

Expandable graphite was first converted to expanded graphite (ExG) by an isothermal treatment at 900 °C for 1 min. The ExG/PEG CPCMs were fabricated by stirring proper amounts of ExG in PEG–ethanol solution containing appropriate quantities of PEG for 2 hours. This stirring step allowed PEG to well disperse in the porous network of ExG. Afterwards, the mixtures were heated to 80 °C to remove the solvent. After this step, PEG was partially deposited inside the pores of ExG, and some PEG might still adsorb on the external surfaces of ExG. Thus, the ExG/PEG mixtures were further treated at 80 °C (above the melting point of PEG) for 24 hours to maintain PEG in the liquid phase, allowing PEG to be adsorbed into ExG's pores by the capillary effect. By this method, four ExG/PEG CPCMs with PEG contents of 60, 70, 80, and 90% were fabricated. They were abbreviated as CPCM*x*, with *x* denoting the PEG content.

2.3 Characterization methods

Scanning electron microscopy (SEM) images were measured using a Hitachi S-4800 instrument (Japan). Fourier-transform infrared (FTIR) spectra were measured using a JASCO FTIR 4600 instrument (Japan). X-ray diffraction (XRD) patterns were measured using a Bruker D2 Phaser instrument (Germany). Differential scanning calorimetry (DSC) curves were measured using a NETZSCH 214 Polyma instrument (Germany). Thermogravimetric analysis (TGA) curves were measured using a Setaram Labsys Evo TG-DSC 1600 analyzer (France). Thermal conductivities were obtained using a Hot Disk TPS 2500S instrument (Sweden). The electrical conductivity was obtained by a 2-probe resistivity measurement following ref. 38, 39, using a high-sensitivity Keithley 2400 Digital Multimeter at a fixed current of 100.000 mA.

3. Results and discussion

3.1 Microstructure, chemical compatibility, and crystallization behaviors

Fig. 1 shows the SEM images of the pristine ExG and fabricated CPCMs. The pristine ExG (Fig. 1a) was formed by the stacking of multiple graphene layers, generating a three-dimensional (3D) porous structure. The pores of ExG were minor in micropores and abundant in meso- and macropores, with a total pore volume of up to 40 cm^3 g^{-1} and a surface area of up to 200 m^2 g^{-1}, allowing the infiltration of large amounts of PCMs.[13,40] When ExG was combined with 60% PEG (Fig. 1b), its porous network could not be seen clearly because of the intrusion of PEG. With increasing PEG to 70, 80, and 90% (Fig. 1c–e), the porous network of ExG was further occupied by PEG. These results indicated successful infiltration of PEG into the ExG porous structure.

The FT-IR method was used to characterize the chemical compatibility of PEG in the fabricated CPCMs, as shown in Fig. 2a. The pristine ExG almost showed no absorption due to its lack of a dipole moment, consistent with the reported literature.[41,42] Meanwhile, the pure PEG exhibited three characteristic absorption peaks at 3446, 2888, and 1108 cm^{-1}, corresponding to the stretching vibrations of –OH, $–CH_2$, and –C–O groups, respectively.[20,43] Notably, the two typical composites (CPCM70 and CPCM90) fully possessed the characteristic absorption peaks at the same positions as pure PEG, indicative of a physical combination of PEG and ExG.

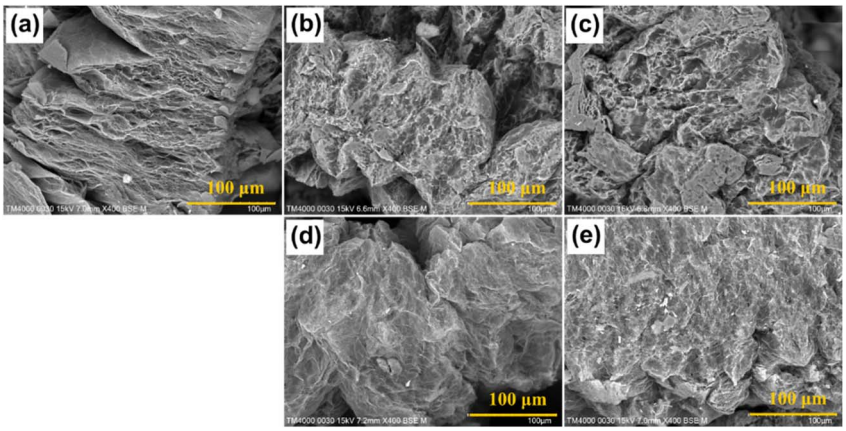

Fig. 1 SEM images of (a) EG, (b) CPCM60, (c) CPCM70, (d) CPCM80, and (e) CPCM90.

The XRD method was used to study the crystallization behaviours of PEG confined in the CPCMs, as shown in Fig. 2b. The pristine ExG exhibited a diffraction peak at 2θ of 26.4°, typically for a graphite-based material.[44,45] The pure PEG exhibited two characteristic diffraction peaks at 2θ of 19.2 and 23.3°, consistent with the reported literature.[23,46] Notably, the two typical composites showed combined diffraction peaks of PEG and ExG at the same diffraction angles, and the two peaks derived from PEG were in the same intensity ratio as those in pure PEG. These results indicated that the crystallization behaviours of PEG were unchanged in the composites.

3.2 Heat storage behaviors

The DSC method was used to study the heat storage behaviors of the fabricated CPCMs, and the obtained DSC thermograms are shown in Fig. 3a and b. Both pure PEG and the fabricated CPCMs exhibited one endothermic peak during the melting with a small shoulder at a lower temperature and one exothermic peak during the crystallization. Compared to pure PEG, the fabricated CPCMs showed slightly lower melting (T_M) and crystallization (T_C) temperatures by below 0.5 and 2.7 °C, respectively, as shown in Fig. 3c. The lowered phase change temperature of a PCM confined in a porous network was a commonly observed phenomenon and attributed to the confinement effects in nano-spaces.[47,48] According to the Gibbs–Thomson equation, the phase change temperature depression increases with decreasing pore size of porous supports.[49,50] Several porous supports with small pores (<20 nm) could cause the depression of 2.5–7 °C.[49,51] In this work, because the pores of ExG were mainly meso and macropores, the phase change temperatures were slightly depressed.

As shown in Fig. 3d, the fabricated CPCMs exhibited melting/crystallization enthalpies lower than pure PEG, and the values increased with increasing PEG contents, reaching ~151 J g^{-1} for the CPCM90. These can be readily understood by that the phase change enthalpies of the CPCMs were only derived from PEG. As a result, increasing PEG content led to increased phase change enthalpies. Additionally, previous reports showed that strong interfacial interactions, *e.g.*, hydrogen bonding, between PEG and porous supports could restrict the free mobility of PEG and result in suppressed crystallinity.[52,53] The crystallinity of a PCM confined in a CPCM is usually evaluated by estimating the crystallization fraction (F, (%)) using eqn (1):[24,48]

$$F = \frac{\Delta H_{M,CPCM} \times 100}{\Delta H_{M,PCM} \times x} \quad (1)$$

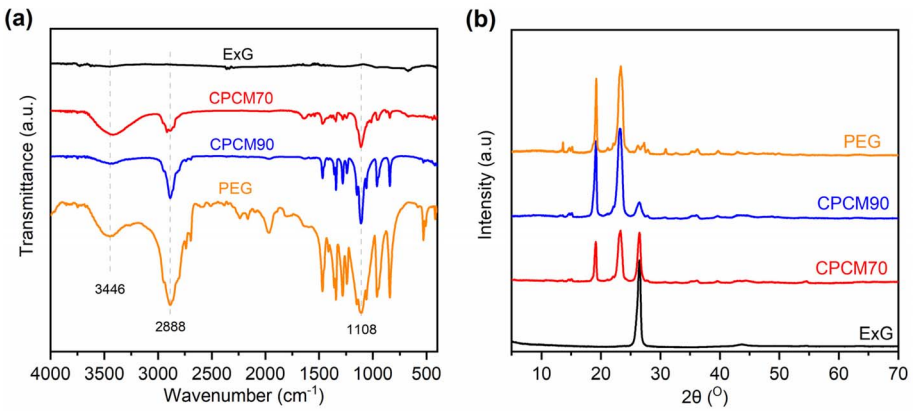

Fig. 2 (a) FTIR spectra and (b) XRD patterns of EG, PEG, CPCM70, and CPCM90.

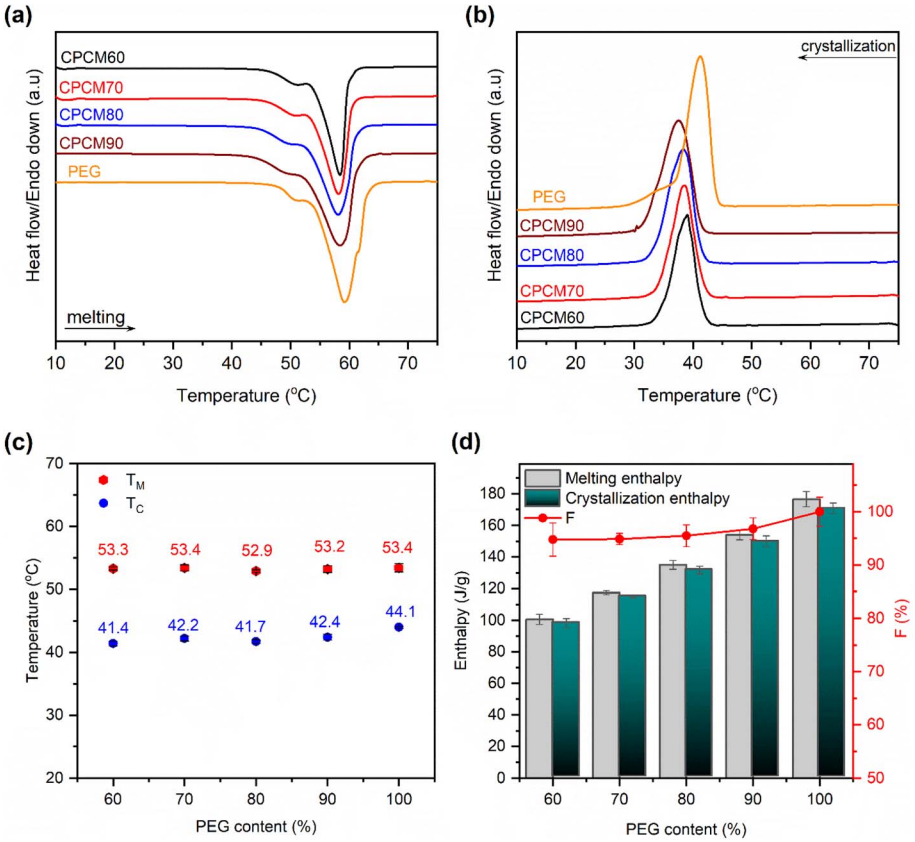

Fig. 3 (a) Melting DSC curves, (b) crystallization DSC curves, (c) phase change temperatures, and (d) phase change enthalpies of PEG and the fabricated CPCMs.

where $\Delta H_{M,CPCM}$ and $\Delta H_{M,PCM}$ are the melting enthalpies of the fabricated CPCM and pure PCM, respectively, and x is the mass ratio of PCM in the CPCM. As shown in Table 1, the crystallinity of PEG was completely suppressed as confined in SiO_2-based materials, including SBA-15 (0%) and MCM-41 (0%), due to interfacial hydrogen bonding, with the F values shown in the parentheses. The suppressed crystallinities quenched the phase change ability, causing zero phase change enthalpies for the corresponding CPCMs. Notably, the fabricated CPCM60–CPCM90 exhibited very high crystallization fractions of 94.8–

Table 1 Thermophysical properties of the fabricated CPCMs compared to reported CPCMs

CPCMs	PEG content (%)	F (%)	ΔH_M (J g^{-1})	TC (W m^{-1} K^{-1})	Ref.
PEG/SBA-15	70	0	0	—	52
PEG/MCM-41	70	0	0	—	53
PEG/activated carbon	80	79.4	102	—	54
PEG/mica	46.24	98.5	77.75	0.59	16
PEG/fumed silica	80	93.1	130.6	0.18	55
PEG/silica hydroxyl	70.0	91.3	105.3	0.37	56
PEG/modified rice husk ash	62.1	97.7	119.3	0.35	57
PEG/diatom biomass	72.5	89.5	121.5	—	58
PA/ExG/SEBS[a]	58.3	100	137.7	2.87	5
SAT/(ExG)/borax/CMC[a]	93	—	119.7	2.456	4
SA/EG/Fe_3O_4[a]	80	98.4	152.4	3.965	59
SAT/ExG/borax/PAM/CS/SEBC[a]	50	100	130.7	1.152	60
CPCM60	60	94.4	96.4	7.657	This work
CPCM70	70	94.9	113.1	6.178	This work
CPCM80	80	98.2	133.6	4.602	This work
CPCM90	90	98.7	151.1	3.207	This work

[a] Reported CPCMs used for thermotherapy applications.

96.8% (Fig. 3d). This was because there was almost no hydrogen bonding between PEG and EG since EG surfaces had virtually no functional groups, as demonstrated in the FTIR results. The *F* values of the fabricated CPCMs in this work were comparable or even exceeded the other CPCMs shown in Table 1, including PEG/activated carbon (79.4%), PEG/mica (98.5%), PEG/fumed silica (93.1%), silica hydroxyl (91.3%), PEG/modified rice husk ash (97.7), PEG/diatom biomass (89.5%), paraffin/ExG/styrene ethylene butylene styrene (PA/ExG/SEBS, 100%), stearic acid/ExG/Fe_3O_4 (SA/ExG/Fe_3O_4, 98.4%), and sodium acetate trihydrate/ExG/borax/polyacrylamide/chitosan/SEBC (SAT/ExG/borax/PAM/CS/SEBC, 100%). It can be said that a meaningful advantage of EG over the other porous supports is the ability to maintain a high crystallinity for PEG. It is noted that the crystallization fractions of PEG in the fabricated CPCMs could not reach 100% because the mobility of PEG was still disturbed to some extent when combined with EG as a solid substance.

3.3 Thermal stability and thermal conductivity

Fig. 4a exhibits the thermal stability of the fabricated composites compared to pure PEG, characterized by TGA. The fabricated composites showed thermal decomposition behaviours quite similar to pure PEG. Specifically, they showed excellent thermal stability with almost no weight loss at temperatures up to 375 °C. At higher temperatures, they showed a one-step weight loss within 375–445 °C due to the decomposition of PEG. The weight loss of the prepared CPCM60, CPCM70, CPCM80, and CPCM90 was obtained at 59.2, 70.2, 79.8, and 90.6%, which were consistent with the doped PEG amounts. Notably, the charging temperatures applied to the fabricated CPCMs during practical usage in thermotherapy are usually just above their melting points (~53 °C). These temperatures were far below their thermal decomposition temperatures (>375 °C), thus assuring a good thermal stability for the CPCMs.

Fig. 4b shows the thermal conductivities (TC) of the fabricated CPCMs compared to pure PEG. The low thermal conductivity of pure PEG (0.275 W (m^{-1} K^{-1})) was tremendously enhanced in the form of CPCMs (3.201–7.683 W (m^{-1} K^{-1}), with factors of 11.6–27.9 times. The thermal conductivity of the CPCMs increased with increasing ExG content due to the superior thermal conductivities of ExG (up to 470 W (m^{-1} K^{-1})).[61,62] This result was in good agreement with the reported literature,[13,34,63] showing the thermal conductivities of CPCMs with 12–14% ExG could be 17–30 times higher than the pure PCMs. The thermal conductivity of the fabricated CPCM90 (the CPCM with the highest thermal energy storage capacity and good leakage resistance (see section 3.4)), outperformed those of other PEG-based CPCMs in Table 1, including PEG/Mica (0.59 W (m^{-1} K^{-1})), PEG/fumed silica (0.18 W (m^{-1} K^{-1})), silica hydroxyl (0.37 W (m^{-1} K^{-1})), PEG/modified rice husk ash (0.35 W (m^{-1} K^{-1})). Compared to reported CPCMs used for thermotherapy applications, it was slightly lower than SA/EG/Fe_3O_4 (3.965 W (m^{-1} K^{-1})) and significantly higher than PA/ExG/SEBS (2.87 W (m^{-1} K^{-1})), SAT/(ExG)/borax/CMC (2.465 W (m^{-1} K^{-1})), and SAT/ExG/borax/PAM/CS/SEBC (1.152 W (m^{-1} K^{-1})) (Table 1).

3.4 Leakage-proof ability and cycling durability

The leakage-proof ability of the fabricated composites compared to pure PEG was examined by a thermal treatment at 70 °C for 60 min. Fig. 5 exhibits the digital photos of the samples during the experiment, from which it can be seen that

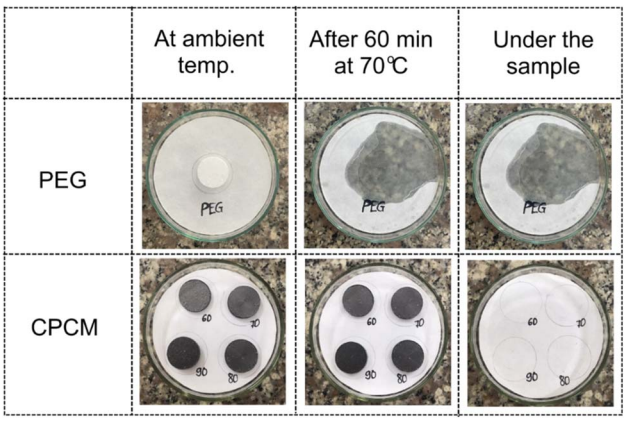

Fig. 5 Digital images of PEG and the fabricated CPCMs during the leakage-proof ability experiment.

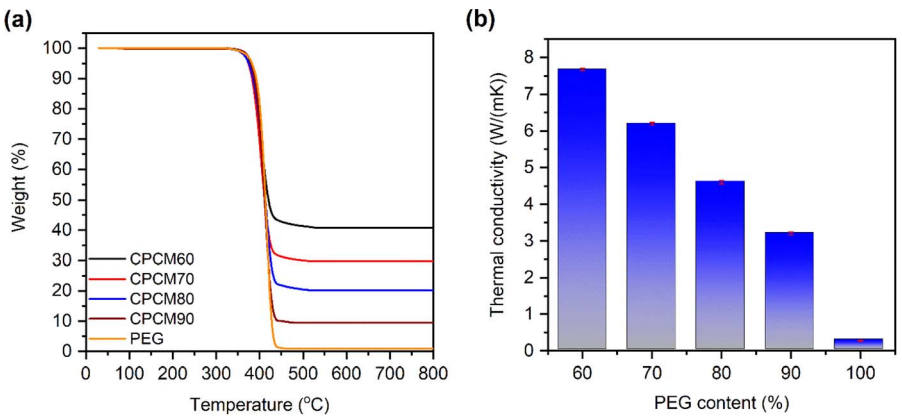

Fig. 4 (a) TGA curves and (b) thermal conductivities of PEG and the fabricated CPCMs.

pure PEG was completely melted and liquidized after the thermal treatment. At the same time, the fabricated CPCMs, even at 90% PEG, exhibited no observable liquid leakage, indicative of good leakage-proof ability. Within the CPCMs, the 3D porous network of ExG with a large pore volume generated capillary and surface tension forces to detain a large amount of PEG, thus preventing the liquid leakage. This result was consistent with those in the reported literature, showing that ExG was capable of detaining up to 90–95% PCMs without leakage.[64–66] The high PEG loading and high crystallization fraction promoted the energy storage capacity for the CPCMs. Indeed, the CPCM90 exhibited the highest melting enthalpy among those listed in Table 1.

Based on the above results, the CPCM90 exhibited high thermal energy storage capacity, high thermal conductivity, and good leakage-proof ability. It was further evaluated for cycling durability for 500 charge/discharge cycles. Fig. 6 shows the results of the cycling durability test characterized by DSC, FTIR, and XRD methods. As shown in the DSC curves (Fig. 6a), after the multiple charge/discharge cycles, the T_M and T_C of the sample were slightly changed by 0.7–1.0 °C. Specifically, the T_M was changed by 0.2, 0.2, and 0.7 °C, and the T_C was changed by 1.0, 1.0, and 0.9 °C after 100, 300, and 500 cycles, respectively. The melting and crystallization enthalpies were only decreased by 4.8 and 4.3 J g^{-1}, corresponding to 3.2 and 2.9%, respectively. Specifically, after 100, 300, and 500 cycles, the ΔH_M decreased by 1.5, 3.3, and 4.8 J g^{-1}, and the ΔH_C decreased by 1.5, 2.8, and 4.3 J g^{-1}, respectively. The XRD (Fig. 6b) and FTIR (Fig. 6c) results of the sample after 500 cycles also exhibited similar absorption and diffraction peaks as those of the first cycle. The DSC, XRD, and FTIR results demonstrated good chemical stability for the composite, generating highly reliable cycling durability for repeated utilization.

3.5 Electrothermal conversion and storage performance

Fig. 7a exhibits the electrical conductivities of the fabricated CPCMs. The electrical conductivity increased with increasing ExG content in the CPCM, ranging from 107.2 to 356.1 S m^{-1} with ExG content 10–40%, corresponding to the PEG content of 90–60%. These values were consistent with a previous report showing that CPCMs with ExG content of 5–15% exhibited electrical conductivities of 66.6–163.9 S m^{-1}.[5] The increased electrical conductivity with ExG content could be readily understood as ExG possesses extremely high electrical conductivity (~10^8–10^{10} (S m^{-1}), while PEG is a kind of electrical insulator.[38,62] Increasing ExG content in the CPCMs would increase the contact possibility between ExGs, leading to increased electrical conductivity. This trend was also observed in the reported literature.[5,38,67]

The Joule heating effect happens when a current flows through a conductive material, and the produced heat (Q) is directly proportional to the square of the current (I^2), the

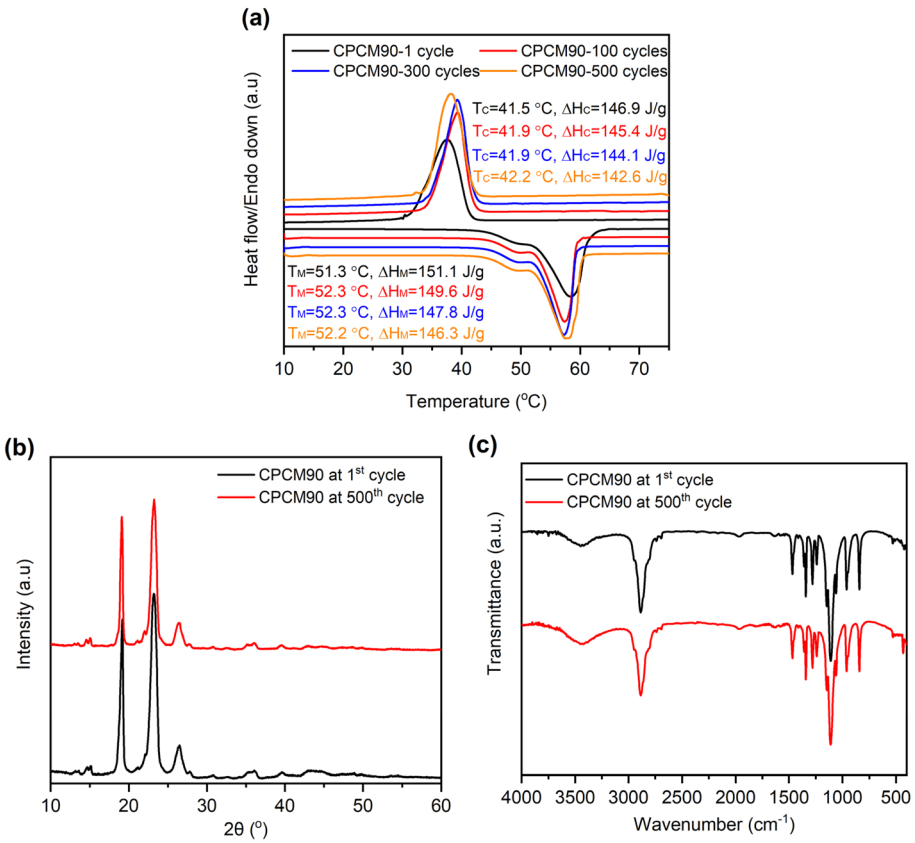

Fig. 6 (a) DSC curves, (b) XRD patterns, and (c) FTIR spectra of the CPCM90 at the first and 500th melting/crystallization cycles.

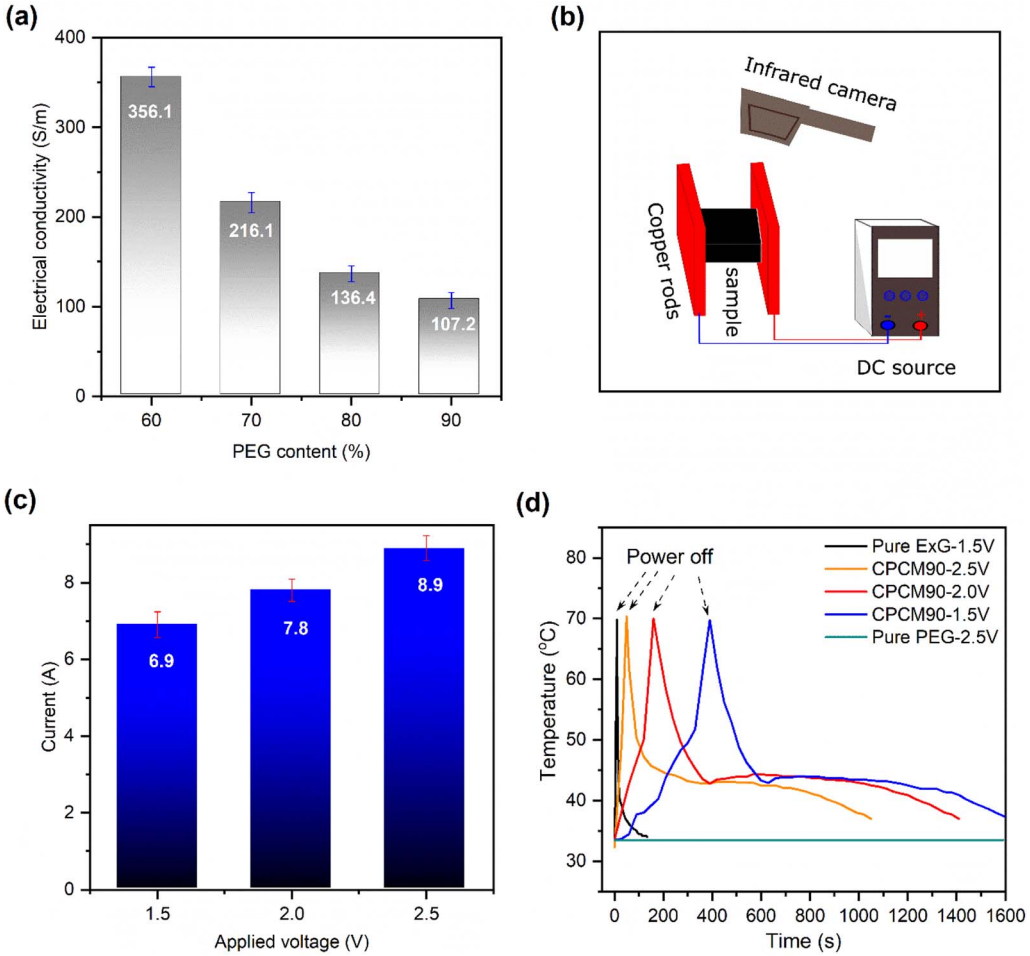

Fig. 7 (a) Electrical conductivities of the fabricated CPCMs, (b) image of eletrothermal test apparatus, (c) the currents at various applied voltages of the fabricated CPCM90, and (d) temperature–time curves at various applied voltages of the fabricated CPCM90 compared to pure ExG and pure PEG.

resistance (R), and the flowing time (t) by the formula: $Q = I^2.R.t$.[3,68] This opens an electrothermal conversion and storage strategy for electrically conductive phase change composites, in which a large amount of produced Joule heat can be stored in the composite in the form of latent heat. In this work, the electrothermal conversion and storage of the CPCM90 were evaluated by applying various voltages (1.5, 2.0, and 2.5 V) using a DC power source, as depicted in Fig. 7b. As shown in Fig. 7c, the currents flowing through the CPCM90 increased with increasing applied voltages and were obtained at 6.9–8.9 A. These values were significantly higher than those of reported composites, including polyethylene glycol/biomass porous carbon (0.721–1.674 A at 1.5–3.0 V)[69] and polyethylene glycol/carbon foam@Co-functionalized MOF (0.26 A at 2.5 V).[3] The high currents accelerated the electrothermal conversion for the sample. As shown in Fig. 7d, the temperature of the CPCM90 could surpass its melting temperature (~53 °C) and reach 70 °C after 390 s, as applied with a voltage as low as 1.5 V. The heating rate increased with increasing applied voltages to 2.0 and 2.5 V, with the time to reach 70 °C of 160 and 50 s, respectively.

As shown in Fig. 7d, when the temperature of CPCM90 reached its melting temperature during the electrical heating, the produced Joule heat was mainly stored in the sample as melting latent heat. Turning off the power caused the sample's temperature to drop quickly due to a large temperature gap with the ambient. When the temperatures decreased to the CPCM90's crystallization point (~42 °C), the crystallization happened, and the accompanying latent heat was released, forming a temperature platform. These results demonstrated excellent electrothermal conversion and storage for the CPCM90, which was attributed to the high electrical conductivity of ExG. Indeed, when pure ExG was applied with a voltage as low as 1.5 V, its temperature was rapidly increased to 70 °C in only 11 s (Fig. 7d). For comparison, the temperature of pure PEG could not be elevated even when applied with a voltage of 2.5 V due to its non-conductive nature (Fig. 7d).

3.6 Photothermal conversion and storage performance

The sunlight is an ideal source of energy for its abundant, green, and renewable properties. The integration of a CPCM with a photothermal conversion ability allows the storage of a large amount of solar energy in the CPCM *via* its high latent heat.[3,27] Herein, the photothermal conversion and storage of the

fabricated CPCM90 were examined under a simulated sunlight of 1000 W m^{-2} using a halogen lamp, as depicted in Fig. 8a. The temperatures under the sample during the experiment were recorded and exhibited in Fig. 8b. The temperatures of the sample could rise to 70 °C after 920 s of illumination, indicative of excellent photothermal conversion. The photothermal conversion efficiency (η) can be estimated using eqn (2):[3,21]

$$\eta = \frac{m\Delta H}{IS(T_e - T_s)} \quad (2)$$

where m (g) is the weight of sample, ΔH (J g^{-1}) is the melting enthalpy of sample, I (W m^{-2}) is the intensity of solar simulator, S (m^2) is the sample's area subjected to solar illumination; and T_s and T_e (s) represent the starting and ending time of the melting process, respectively. The η value for the CPCM90 was calculated to be as high as 84.0%. Meanwhile, pure PEG exhibited a poor photothermal conversion ability, with its temperature increasing to only 48.5 °C at the same illumination intensity and duration. These results were consistent with an effective VIS/NIR absorption of the CPCM90 compared to pure PEG, as shown in Fig. 8c. The high photothermal conversion performance of CPCM90 was mainly derived from the presence of ExG. The sp^2 hybridized carbon system of ExG promoted the capture and conversion of photons from the sunlight to thermal energy. In addition, the high thermal conductivity of CPCM90 facilitated fast and even transfer of heat during the illumination, further enhancing the photothermal conversion.

The temperature–time curve of CPCM90 (Fig. 8b) during the solar illumination was observed with a fast temperature increment at the beginning. At this time, the temperature increment was driven by the conversion of solar energy into sensible heat. When the temperature reached the sample's melting point, a great amount of solar energy was stored in the form of latent heat, which slowed down the temperature-increasing rate and formed a temperature plateau. After the melting was complete, the temperature was accelerated again by the sensible heat. When the solar illumination was stopped, the sample's temperature quickly dropped due to a large temperature gap with the ambient. As the temperature went down to the sample's crystallization point, a temperature plateau was observed due to the crystallization heat release. Overall, these results demonstrated good photothermal conversion and storage/release for the CPCM90.

3.7 Practical thermotherapy performance

The thermotherapy performance of the CPCM90 was practically evaluated in the form of a heat eye-patch, as described as

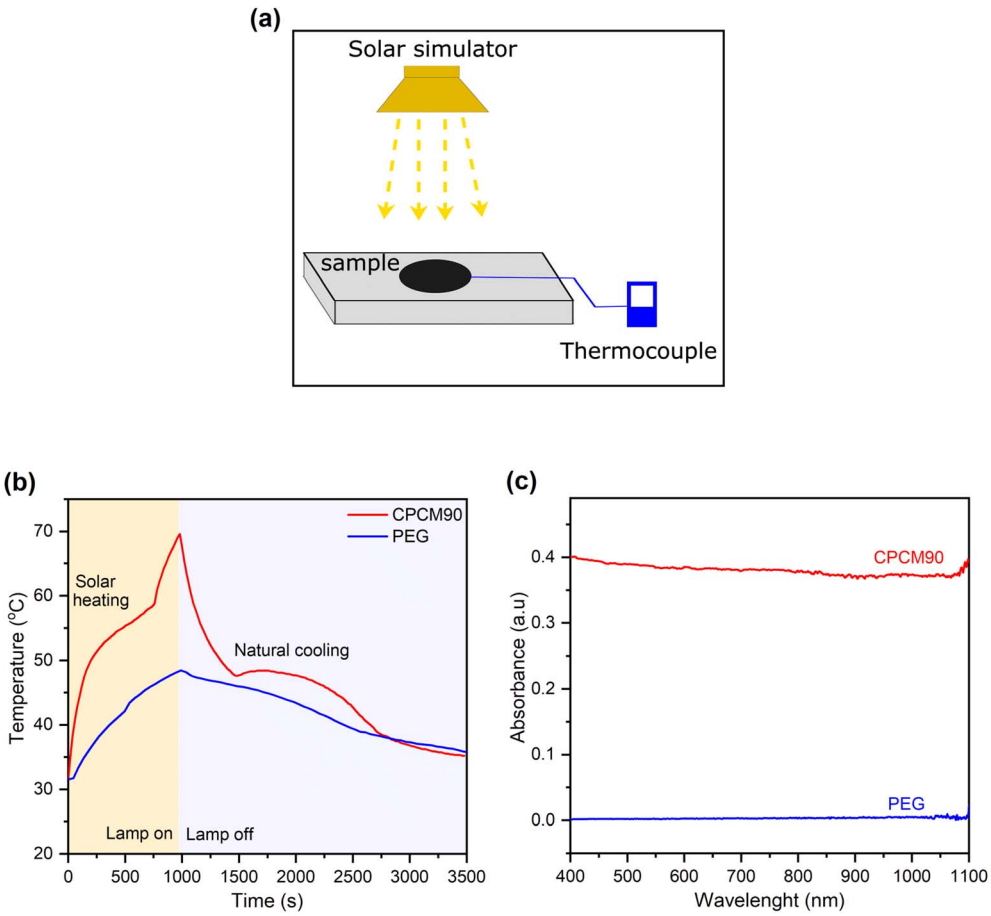

Fig. 8 (a) Image of solarthermal test apparatus, (b) temperature–time curves of the fabricated CPCM90, PEG, and (c) VIS/NIR spectra of the fabricated CPCM90 and PEG.

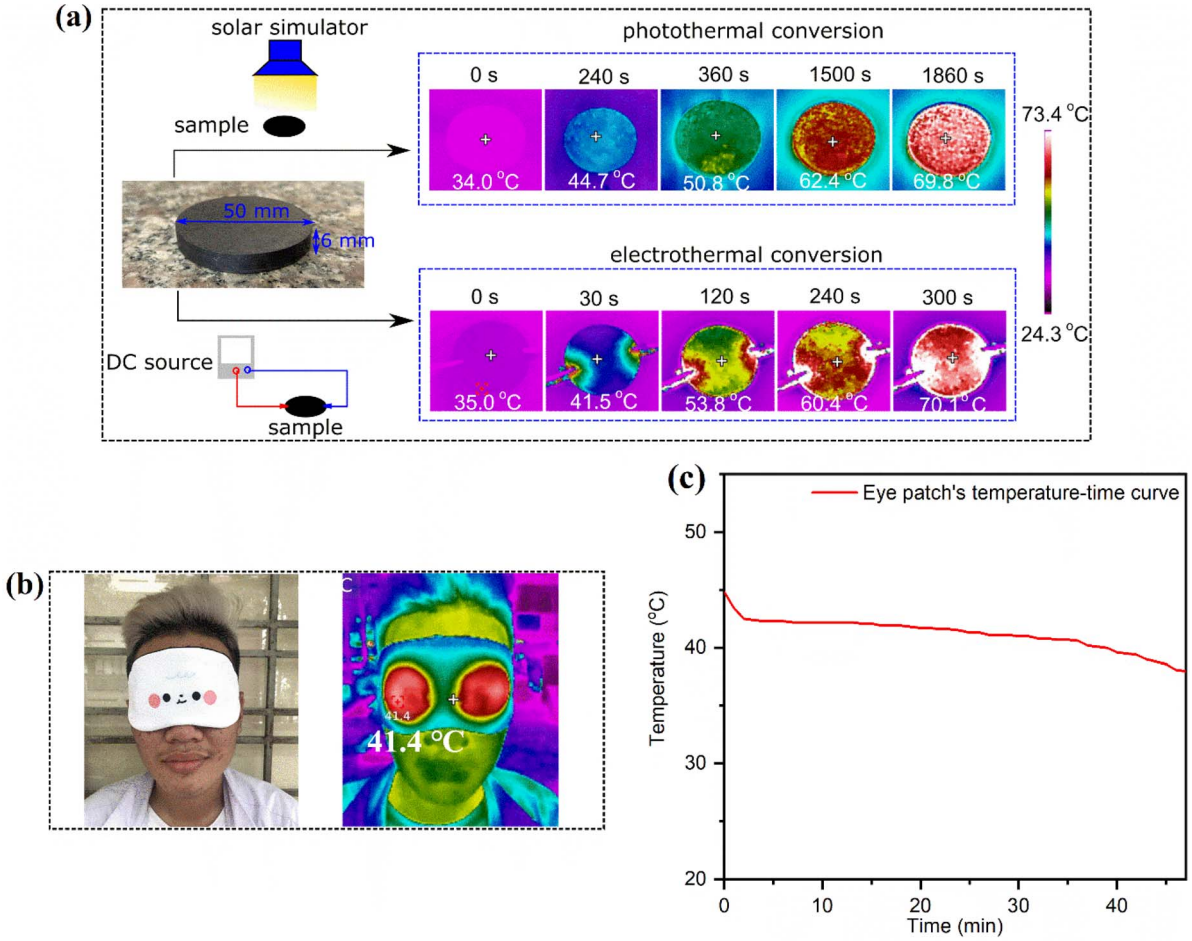

Fig. 9 (a) Image of a round block fabricated from the CPCM90 and its infrared images during photothermal and electrothermal charging, (b) digital and infrared images of the heat eye-patch during the test, and (c) temperature–time curve of the heat eye-patch during the test.

follows. The CPCM90 sample (30 g) was compressed into two round blocks (15 g for each block) with a diameter of 50 mm and a thickness of 6 mm (Fig. 9a). Before usage, the blocks needed to be charged to store latent heat during the melting of CPCM90 by heating them to ~70 °C. Herein, we demonstrated that the blocks could be charged by either photothermal conversion or electrothermal conversion effects. The photothermal charging was conducted by illuminating the blocks at an intensity of 1000 W m^{-2} using a solar simulator, and the electrothermal charging was conducted by applying a DC power of 2.5 V to the blocks through crocodile clips (Fig. 9a). The infrared images of a block during the charging are shown in Fig. 9a, from which it can be seen that the block was effectively heated by both electric and solar power. In comparison, the electrothermal charging (300 s) was faster than the photothermal charging (1860 s), with the time needed to bring the block to ~70 °C shown in the parentheses.

It is noted that the heat charging methods (photothermal or electrothermal charging) of the eye-patch were assumed not to affect the thermotherapy efficacy because the thermotherapy applications were used during the heat discharge of the eye–patch. Herein, we used the blocks heated by the photothermal effect as an example for further practical thermotherapy evaluation. The heated blocks were inserted into an eyeshade to form a heat eye-patch. When the temperature of the heat eye-patch decreased to ~45 °C, it was attached to the eyes of a volunteer. Digital and infrared images of the heat eye-patch during the test are shown in Fig. 9b. The temperature variations of the heat eye patch after being attached to the volunteer were monitored and shown in Fig. 9c. As seen, when the temperature of the heat eye patch decreased to its crystallization point (~43 °C), it started to release the latent heat, forming a long temperature platform. The heat eye-patch maintained temperatures within 42.5–40 °C for an excellent duration of up to 37 min. This temperature range and duration were highly desired for eye relaxation and therapy of some eye issues, such as Meibomian Gland Dysfunction.[37,70] Compared to commercial heat eye patches based on the oxidation of iron powder, the one using CPCM90 was reusable and environmentally friendly.

4. Conclusion

In this study, ExG/PEG CPCMs were fabricated, where ExG served as the porous support and PEG played the role of a thermal energy storage medium. This work concentrated on studying the thermal properties, photo/electrothermal

conversion and storage, and potential application of the CPCMs in thermotherapy. The key findings are listed below:

(1) ExG provided sufficient space to stabilize up to 90% PEG without a liquid phase leakage while maintaining high crystallinities for PEG (94.4–98.7%), thus promoting a high thermal energy storage capacity of 151.1 J g^{-1}. The CPCMs possessed high thermal stability and good cycling durability after 500 melting/crystallization cycles. In addition, the thermal conductivities of the fabricated CPCMs were 11.6–27.9 times higher than that of pure PEG.

(2) ExG possessed both high electrical conductivity and high solar absorption, endowing an effective electro/photothermal conversion and storage for the CPCMs. The CPCM90 could be thermally charged by applying either a low energy of 1.5 V or a simulated solar radiation of 1000 W m^{-2}, with a photothermal conversion efficiency obtained at 84.0%.

(3) The CPCM90 exhibited high performance in practical thermotherapy in the form of a heat eye-patch. It could maintain temperatures within 40.0–42.5 °C for 37 min, which was highly appropriate for eye relaxation and therapy of some eye issues.

Informed consent statement

The ethics responsibility is informed and acknowledged to all the authors and volunteers as a part of content of right of informed consent.

Conflicts of interest

The authors declare no known competing interests.

Data availability

All data generated or analyzed during this study are included in this article.

Acknowledgements

This research is supported by the Ho Chi Minh City University of Technology and Education, Vietnam.

References

1 Z.-R. Li, N. Hu and L.-W. Fan, *Energy Storage Mater.*, 2023, **55**, 727–753.
2 R. Naveenkumar, M. Ravichandran, V. Mohanavel, A. Karthick, L. S. R. L. Aswin, S. S. H. Priyanka, S. K. Kumar and S. P. Kumar, *Environ. Sci. Pollut. Res.*, 2022, **29**, 9491–9532.
3 Y. Li, H. Yu, P. Liu, X. Diao, Y. Feng, Y. Jiang and X. Chen, *SusMat*, 2024, **4**, e214.
4 Y. Li, X. Wu, Y. Liao, H. Shao, Y. Chen, W. Yang, P. Lv, Y. Zhou and C. Tang, *Polymer*, 2024, **305**, 127171.
5 X. Lin, Z. Ling, X. Fang and Z. Zhang, *Appl. Energy*, 2022, **327**, 120141.
6 G. Duttaluru, P. Singh, A. Kumar Ansu, R. kumar Sharma, A. kumar and S. Mishra, *Mater. Today Proc.*, 2022, **63**, 685–691.
7 M. F. Junaid, Z. u. Rehman, M. Čekon, J. Čurpek, R. Farooq, H. Cui and I. Khan, *Energy Build.*, 2021, **252**, 111443.
8 S. L. Tariq, H. M. Ali, M. A. Akram, M. M. Janjua and M. Ahmadlouydarab, *Appl. Therm. Eng.*, 2020, **176**, 115305.
9 B. Eanest Jebasingh and A. Valan Arasu, *Energy Storage Mater.*, 2020, **24**, 52–74.
10 M. M. Umair, Y. Zhang, K. Iqbal, S. Zhang and B. Tang, *Appl. Energy*, 2019, **235**, 846–873.
11 Y. Zhou, J. Zeng, Y. Guo, H. Chen, T. Bi and Q. Lin, *Appl. Energy*, 2023, **352**, 121995.
12 H. Zhang, K. Wang, L. Wang, H. Xie and W. Yu, *Sol. Energy*, 2020, **201**, 628–637.
13 J. Lao, W. Fu, L. Chen, J. Ma, J. Xiang, J. Liu, H. Peng and Y. Luo, *Chem. Eng. J.*, 2024, **497**, 154867.
14 Z. Li, D. Pan, Z. Han, D. J. P. Kumar, J. Ren, H. Hou, Z. M. El-Bahy, G. A. M. Mersal, B. B. Xu, Y. Liu, C. Liu and M. M. Ibrahim, *Adv. Compos. Hybrid Mater.*, 2023, **6**, 224.
15 L. Chen, L. Luo, Z. Mao, B. Wang, X. Feng and X. Sui, *ACS Appl. Mater. Interfaces*, 2024, **16**, 4089–4098.
16 D. Zhang, C. Li, N. Lin, B. Xie and J. Chen, *Int. J. Miner. Metall.*, 2022, **29**, 168–176.
17 S. Karaman, A. Karaipekli, A. Sarı and A. Biçer, *Sol. Energy Mater. Sol. Cells*, 2011, **95**, 1647–1653.
18 B. Kalidasan, A. K. Pandey, R. Saidur, T. K. Han and Y. N. Mishra, *Mater. Today Sustain.*, 2024, **25**, 100634.
19 X. Lu, H. Huang, X. Zhang, P. Lin, J. Huang, X. Sheng, L. Zhang and J.-p. Qu, *Compos. B. Eng.*, 2019, **177**, 107372.
20 W. Luo, M. Zou, L. Luo, Y. Ma, W. Chen, X. Hu, Q. Li and X. Jiang, *J. Energy Storage*, 2024, **78**, 109950.
21 C. Liu, L. Wang, Y. Li, X. Diao, C. Dong, A. Li and X. Chen, *J. Colloid Interface Sci.*, 2024, **657**, 590–597.
22 K. B, A. K. Pandey, R. Saidur and V. V. Tyagi, *J. Energy Storage*, 2023, **58**, 106361.
23 S. Xiao, M. Zou, Y. Xie, W. Chen, X. Hu, Y. Ma, S. Zu, Y. Che and X. Jiang, *J. Energy Storage*, 2022, **56**, 105976.
24 X. Chen, H. Gao, G. Hai, D. Jia, L. Xing, S. Chen, P. Cheng, M. Han, W. Dong and G. Wang, *Energy Storage Mater.*, 2020, **26**, 129–137.
25 N. Zheng, H. Pan, Z. Chai, Z. Liu, F. Gao, G. Wang and X. Huang, *ChemSusChem*, 2024, **17**, e202301971.
26 A. M. Darabut, Y. Lobko, Y. Yakovlev, M. G. Rodríguez, K. Veltruská, B. Šmíd, P. Kúš, J. Nováková, M. Dopita, M. Vorokhta, V. Kopecký, M. Procházka, I. Matolínová and V. Matolín, *Adv. Powder Technol.*, 2022, **33**, 103884.
27 C. Liu, Y. Wan, Y. Gao, C. Dong and X. Chen, *Mater. Today Nano*, 2023, **23**, 100376.
28 Y. Huo, T. Yan, X. Chang and W. Pan, *Sol. Energy*, 2023, **263**, 111922.
29 L. Yang, Y. Yuan, N. Zhang, Y. Dong, Y. Sun and W. Ji, *Int. J. Energy Res.*, 2020, **44**, 8555–8566.
30 S. Liu, X. Fei, B. Zhang, H. Zhao and M. Wan, *Sol. Energy Mater. Sol. Cells*, 2022, **236**, 111484.
31 X. Lin, X. Zhang, L. Liu, J. Liang and W. Liu, *J. Cleaner Prod.*, 2022, **331**, 130014.

32 F. Li, H. Zhen, L. Li, Y. Li, Q. Wang and X. Cheng, *Mater. Today Energy*, 2022, **26**, 100999.
33 X. Li, H. Li, X. Kong and H. Yang, *J. Energy Storage*, 2021, **35**, 102326.
34 C. Ao, S. Yan, S. Zhao, W. Hu, L. Zhao and Y. Wu, *Energy Rep*, 2022, **8**, 4834–4843.
35 S. Wu, T. Yan, Z. Kuai and W. Pan, *Sol. Energy*, 2020, **205**, 474–486.
36 R. Ye, W. Lin, X. Fang and Z. Zhang, *Appl. Therm. Eng.*, 2017, **126**, 480–488.
37 R. W. Y. Habash, R. Bansal, D. Krewski and H. T. Alhafid, *Crit. Rev. Biomed. Eng.*, 2006, **34**, 459–489.
38 H. Zhang, Q. Sun, Y. Yuan, Z. Zhang and X. Cao, *Chem. Eng. J.*, 2018, **336**, 342–351.
39 G. Zhou, E. Mikinka, X. Bao and W. Sun, *Funct. compos. mater*, 2023, **4**, 3.
40 R. Goudarzi and G. Hashemi Motlagh, *Heliyon*, 2019, **5**, e02595.
41 K. Luo, D. Wu, Y. Wang, H. Fei, H. Jiang and Z. Ye, *J. Energy Storage*, 2023, **73**, 109151.
42 G. T. Nguyen, T. H. Bui, N. H. Hieu, N. T. C. Tuyen, N. B. Dang, L. T. K. Phung and D. K. Huyen, *J. Energy Storage*, 2024, **100**, 113634.
43 B. Kalidasan, A. K. Pandey, R. Saidur, B. Aljafari, A. Yadav and M. Samykano, *Sustain. Energy Technol. Assess.*, 2023, **60**, 103505.
44 D. Huang, G. Ma, Z. Yu, P. Lv, Q. Zhou, Q. Liu, C. Peng, F. Xiong and Y. Huang, *RSC Adv.*, 2023, **13**, 13252–13262.
45 Y. Xin, H. Nian, J. Li, J. Zhao, X. Tan, Y. Zhou, F. Zhu, H. Liu and X. Li, *J. Energy Storage*, 2022, **46**, 103902.
46 L. Feng, R. Yu, Y. Li, Y. Huang and L. Zhao, *Thermochim. Acta*, 2023, **720**, 179428.
47 W. Aftab, X. Huang, W. Wu, Z. Liang, A. Mahmood and R. Zou, *Energy Environ. Sci.*, 2018, **11**, 1392–1424.
48 H. Gao, J. Wang, X. Chen, G. Wang, X. Huang, A. Li and W. Dong, *Nano Energy*, 2018, **53**, 769–797.
49 T. Nomura, C. Zhu, N. Sheng, K. Tabuchi, A. Sagara and T. Akiyama, *Sol. Energy Mater. Sol. Cells*, 2015, **143**, 424–429.
50 N. Wu, X. Lu, R. An and X. Ji, *Chin. J. Chem. Eng.*, 2021, **31**, 198–205.
51 R. A. Mitran, D. Berger, C. Munteanu and C. Matei, *J. Phys. Chem.*, 2015, **119**, 15177–15184.
52 J. Wang, M. Yang, Y. Lu, Z. Jin, L. Tan, H. Gao, S. Fan, W. Dong and G. Wang, *Nano Energy*, 2016, **19**, 78–87.
53 D. Feng, Y. Feng, P. Li, Y. Zang, C. Wang and X. Zhang, *Microporous Mesoporous Mater.*, 2020, **292**, 109756.
54 L. Feng, W. Zhao, J. Zheng, S. Frisco, P. Song and X. Li, *Sol. Energy Mater. Sol. Cells*, 2011, **95**, 3550–3556.
55 G. T. Nguyen, *RSC Adv.*, 2023, **13**, 7621–7631.
56 K. Sun, Y. Kou, H. Zheng, X. Liu, Z. Tan and Q. Shi, *Sol. Energy Mater. Sol. Cells*, 2018, **178**, 139–145.
57 K. Yu, Y. Liu and Y. Yang, *J. Energy Storage*, 2021, **43**, 103172.
58 J. Huang, B. Wu, S. Lyu, T. Li, H. Han, D. Li, J.-K. Wang, J. Zhang, X. Lu and D. Sun, *Sol. Energy Mater. Sol. Cells*, 2021, **219**, 110797.
59 G. Tien Nguyen, N. Tran Thi, N. Thanh Nho, L. T. Duy Hanh and H. N. Anh Tuan, *J. Sci.: Adv. Mater. Devices*, 2024, **9**, 100792.
60 Y. Li, X. Wu, L. Tang, L. Xie, X. Zeng, S. Wang, K. Liu, M. Xu, C. Tang, W. Yang and D. Han, *ACS Appl. Polym. Mater.*, 2024, **6**, 1460–1469.
61 S. Wu, Q.-Y. Li, T. Ikuta, K. Morishita, K. Takahashi, R. Wang and T. Li, *Int. J. Heat Mass Transfer*, 2021, **171**, 121115.
62 P. Murugan, R. D. Nagarajan, B. H. Shetty, M. Govindasamy and A. K. Sundramoorthy, *Nanoscale Adv.*, 2021, **3**, 6294–6309.
63 T. Wang, Y. Liu, R. Meng and M. Zhang, *J. Energy Storage*, 2021, **34**, 101997.
64 S. Liu, X. Zhang, X. Zhu and S. Xin, *ACS Omega*, 2021, **6**, 17988–17998.
65 G. Fang, M. Yu, K. Meng, F. Shang and X. Tan, *Energy Fuels*, 2020, **34**, 10109–10119.
66 M. Yuan, Y. Ren, C. Xu, F. Ye and X. Du, *Renew. Energ.*, 2019, **136**, 211–222.
67 F. Xue, Y. Lu, X.-d. Qi, J.-h. Yang and Y. Wang, *Chem. Eng. J.*, 2019, **365**, 20–29.
68 M. Weng, J. Lin, Y. Yang, J. Su, J. Huang, X. Lu and X. Sheng, *Sol. Energy Mater. Sol. Cells*, 2024, **272**, 112915.
69 K. Zhou, Y. Sheng, W. Guo, L. Wu, H. Wu, X. Hu, Y. Xu, Y. Li, M. Ge, Y. Du, X. Lu and J. Qu, *Adv. Compos. Hybrid Mater.*, 2023, **6**, 34.
70 D. Borchman, *Ocul. Surf.*, 2019, **17**, 360–364.